Asian Journal of Applied Science and Technology (AJAST)
Volume 10, Issue 3, Pages 01-30, July-September 2026

Non-AI Multipass Edge and Body Pixel Sharpening Pipeline for High-Resolution Lunar Astrophotography Enhancement

Swarnajit Bhattacharya[1*]

[1]*Department of Applied Electronics and Instrumentation Engineering (AEIE), Haldia Institute of Technology, Haldia, Purba Medinipur, West Bengal, India. Corresponding Author Email: swarnabhatta.9@gmail.com*[*]

DOI: https://doi.org/10.38177/ajast.2026.10301

Copyright © 2026 Swarnajit Bhattacharya. This is an open-access article distributed under the terms of the Creative Commons Attribution License, which permits unrestricted use, distribution, and reproduction in any medium, provided the original author and source are credited.

Article Received: 17 May 2026 *Article Accepted: 25 July 2026* *Article Published: 09 August 2026*

ABSTRACT

Processing the lunar astrophotography imagery is challenging since atmospheric turbulence and low-light conditions introduce blur and noise that obscure small-scale lunar features. The present work proposes an enhancement pipeline that operates entirely within classical signal processing, providing a transparent alternative to black-box machine learning methods while remaining practical on standard personal computers. The pipeline integrates four key stages: lucky-imaging frame selection and stacking, wavelet-domain denoising, adaptive local contrast enhancement, and dual-stage edge sharpening. The pipeline is evaluated on 30 lunar datasets spanning multiple phases and multiple observable conditions. Quantitative results show Peak Signal-to-Noise Ratio (PSNR) improvements of approximately 6.2–12.4 dB and an increase in Structural Similarity Index Measure (SSIM) from 0.56 to 0.90, indicating better structural fidelity relative to stacked baselines. Stacking of 16 carefully selected frames yields effective SNR gains of up to about 3.2 times, while modulation transfer function (MTF) analysis at limb and crater-edge boundaries reveals sharpness improvements in the order of 28–35%. The workflow requires no specialized accelerators, with typical resource usage of roughly 4.2 MB memory and 2.3 seconds per megapixel on conventional CPUs. This is demonstrating that classical, interpretable techniques remain highly competitive for scientific and educational lunar image enhancement.

Keywords: Lunar Astrophotography, Image Enhancement, Lucky Imaging, Wavelet Denoising, Contrast Limited Adaptive Histogram Equalization (CLAHE), Multi-Pass Edge Sharpening, Signal-to-Noise Ratio (SNR), Structural Similarity Index (SSIM), Modulation Transfer Function (MTF), Classical Image Processing, Image Stacking, Astronomical Image Restoration.

Graphical Abstract

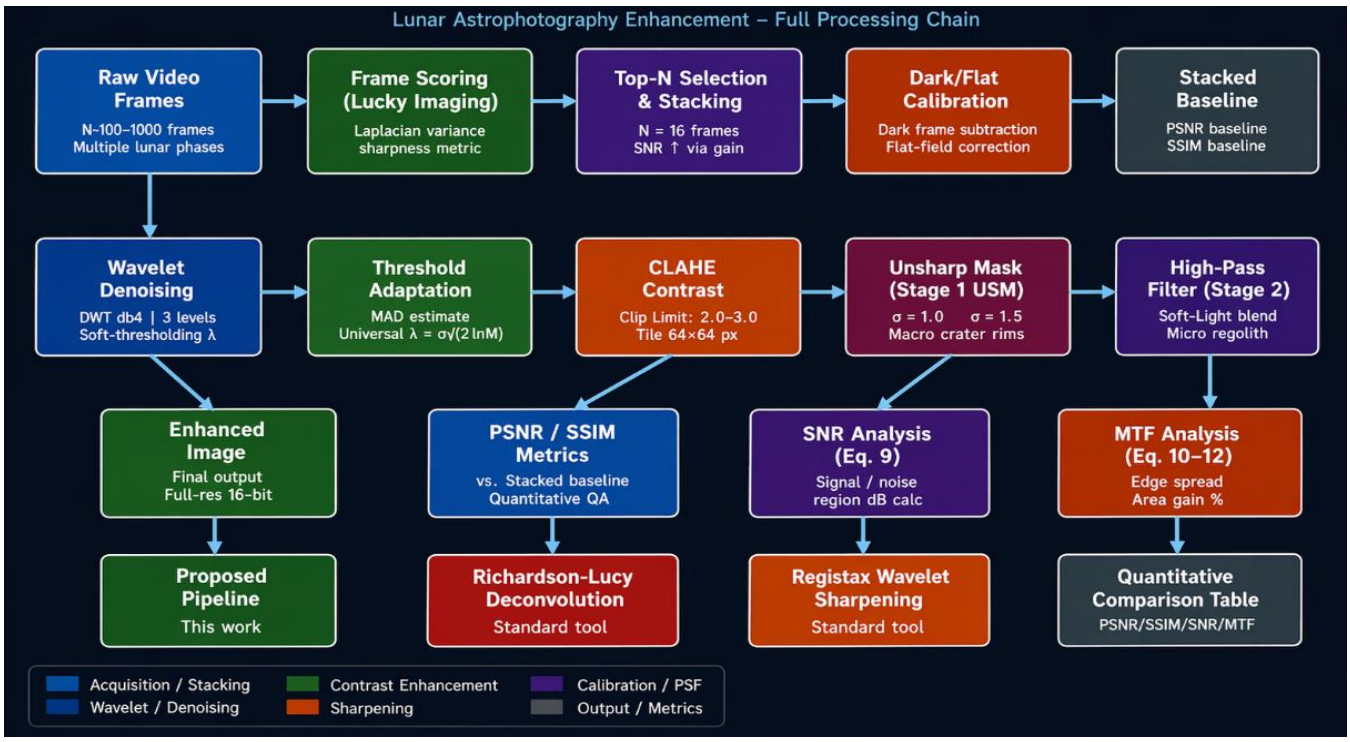

1.0. Literature Review and Introduction

Image enhancement for high-resolution astrophotography has become an essential component of astronomical observation, particularly for lunar surface imaging where atmospheric turbulence, sensor noise, and optical

aberrations present significant challenges to image quality. This literature review examines non-artificial intelligence approaches to enhancing lunar astrophotography, covering fundamental image processing techniques, denoising methods, sharpening algorithms, and quality assessment metrics.

Image registration serves as a fundamental preprocessing stage in astronomical workflows, especially for lunar imaging where feature correspondence is challenging due to illumination variations and surface complexity. Prior comparisons of feature detectors such as SIFT and ORB demonstrate that scale-invariant methods generally provide better robustness for lunar scenes, particularly under varying solar incidence angles that heavily influence terrain contrast and shadow morphology [1]. The importance of accurate astronomical object detection has also been emphasized through advanced multi-stage methods incorporating greyscale adjustments, adaptive background modelling, histogram equalization, and noise-aware Gaussian filtering, enabling significantly higher faint-object detection rates compared to conventional tools such as SExtractor [2]. Wavelet-based denoising remains a cornerstone technique in astronomical imaging, with multi-resolution wavelet thresholding shown to effectively suppress noise while preserving structural information in cosmic background maps and high-resolution images [3]. Extensions combining wavelet transforms with mathematical morphology further improve interference removal in radio astronomy applications while maintaining scientific fidelity [4]. Broader analyses highlight wavelets as a dominant tool for multi-scale feature extraction, although limitations arise for narrow structures when square wavelets are used [5].

Deconvolution continues to play a critical role in image restoration, with the Richardson–Lucy (RL) algorithm being one of the most widely applied due to its flux-preserving and positivity-constrained properties [6]. However, RL's computational inefficiency and susceptibility to noise amplification remain well-documented issues, which motivates accelerated gradient-based strategies and GPU-optimized implementations [6]. RL-based spectral extraction techniques have shown increased resolution and reduced ringing artifacts in large-scale survey data [7], while analytical evaluations demonstrate that RL inherently amplifies high-frequency noise as iterations grow, with peak SNR gains typically occurring after only a few tens of iterations [8]. Broader reviews underscore the necessity of regularization techniques to mitigate RL's convergence instabilities and to prevent the loss of faint sources [9].

Contrast enhancement methods, particularly histogram equalization (HE), have long been employed to improve visibility in low-illumination lunar regions. While traditional HE redistributes intensities for global contrast improvement, it often introduces over-enhancement artifacts, especially in permanently shadowed regions [10]. Contrast Limited Adaptive Histogram Equalization (CLAHE) addresses these issues by operating on local blocks while restricting amplification of noise, making it more suitable for lunar surfaces exhibiting extreme lighting variability [11]. Adaptive contrast manipulation also plays a central role in compositional mapping from Apollo X-ray observations, where careful weighting reveals subtle geochemical variations [12]. Sharpening techniques such as unsharp masking provide effective enhancement of fine lunar surface features, though they are known to increase pixel-level noise without improving true angular resolution [13]. Deconvolution sharpening and controlled local contrast adjustments further enhance details but must be applied conservatively to avoid limb over-brightening and loss of photometric accuracy [14]. High-pass filtering offers an alternative by accentuating

high-frequency structures using blend-mode-based contrast boosting, supporting flexible and non-destructive refinement for lunar detail enhancement [15].

Multi-frame image stacking remains one of the most effective strategies for improving signal-to-noise ratio (SNR) in lunar and deep-sky imaging. As stacking averages uncorrelated noise components, SNR increases proportionally to the square root of the number of frames, forming the basis of most astrophotography workflows [16]. Detailed noise models account for photon shot noise, dark current, and read noise and confirm that many short exposures yield lower SNR than a single long exposure of equivalent integration time due to cumulative read noise contributions [17]. Proper exposure length therefore plays a critical role, as images must sufficiently rise above the detector noise floor to maximize dynamic range and minimize read-noise dominance [18].

Accurate modelling of the optical system requires precise characterization of the point spread function (PSF). Studies of space-borne telescopes demonstrate that PSFs can exhibit multi-peaked structures due to diffraction elements such as entrance filter meshes, and fitting functions such as Moffat and Voigt profiles often provide the most accurate representation of the PSF core [19]. Gaussian-like PSFs remain widely used for representing defocus blur, although atmospheric turbulence for ground-based systems introduces anisoplanatic variations that dominate the effective PSF across the field [20]. Atmospheric turbulence correction therefore remains essential, with recent neural network–based methods using short-exposure sequences to remove geometric and blur distortions while preserving photometry even under low SNR conditions [21]. Hardware-based adaptive optics further provide real-time wavefront correction using single or multiple guide stars, significantly expanding corrected fields of view in modern telescopes [22]. Advanced generative diffusion models additionally address turbulence-induced distortions by integrating strong priors for both geometric correction and structure preservation [23].

Complete lunar image-processing workflows combine acquisition, registration, stacking, and enhancement using specialized software pipelines. Tools such as PIPP automate initial sorting, centering, and quality filtering of lunar data [24], while AutoStakkert! performs multi-point alignment and selective stacking for optimal frame integration [25]. Post-stack sharpening is commonly performed using wavelet layers in Registax, enabling fine detail recovery through multi-scale adjustment [26]. Subsequent refinement in image editors with curves, unsharp mask, or high-pass filters provides final tonal and structural optimization [27]. Evaluation of enhancement outcomes typically employs PSNR and SSIM metrics to quantify detail preservation and structural similarity between original and processed frames [28], with additional SNR-based assessments demonstrating the benefits of adaptive enhancement and denoising in extremely low-light lunar regions [29].

Resolution enhancement plays an increasingly important role in modern lunar analysis, with deep learning–based super-resolution networks enabling higher-quality crater extraction from low-resolution DEMs. Such approaches improve small-crater detection accuracy through advanced feature pyramid networks and enhanced multi-scale fusion [30]. Historically, lunar image processing has drawn from pioneering techniques developed during NASA's Ranger and Surveyor missions, which introduced early digital denoising and contrast expansion methods that set the foundation for modern practices [31]. More recent developments include generalized diffusion-based denoising designed to preserve nebular structures and mitigate star-like artifacts [32], along with GPU-optimized frameworks

that accelerate essential pre-processing tasks such as alignment, stacking, background extraction, photometry, and astrometry for time-domain astronomy pipelines [33]. Collectively, these studies demonstrate that non-AI enhancement methodologies remain indispensable, offering transparent, reproducible, and scientifically grounded improvements in lunar astrophotography and astronomical imaging more broadly [34]. In addition to the iterative and spatial-domain methods discussed, classical model-based techniques in the frequency domain provide a robust mathematical framework for image restoration. Wiener filtering serves as a foundational approach in this category, functioning as a linear estimator that minimizes the mean square error (MSE) between the estimated and original image. By incorporating the noise power spectrum and the Point Spread Function (PSF) of the optical system, the Wiener filter effectively balances the inverse filtering of blur with the suppression of noise, preventing the high-frequency amplification typically seen in simpler deconvolution methods. This makes it a reliable choice for restoring lunar features where the atmospheric and sensor noise characteristics can be estimated. [35, 36, 37].

Furthermore, broader Fourier-domain methods utilize the Fast Fourier Transform (FFT) to perform efficient spectral manipulation for enhancement. These techniques allow researchers to apply targeted frequency-selective filters—such as low-pass filters for noise reduction or high-frequency emphasis filters for edge sharpening—with significant computational speed. Because these methods operate on the global frequency components of the image, they provide a transparent and deterministic alternative to modern iterative schemes, ensuring that the processed results remain scientifically verifiable and free from the artifacts often introduced by "black-box" models. [38]

1.1. Study Objectives

1. To develop a transparent, non-AI image enhancement pipeline that integrates lucky imaging, multi-frame stacking, wavelet-based denoising, adaptive contrast enhancement (CLAHE), and multi-pass edge sharpening for improving high-resolution lunar astrophotographs.

2. To enhance the visual quality and scientific fidelity of lunar images by reducing atmospheric turbulence effects, suppressing image noise, and preserving fine surface structures such as craters, rilles, mountain ridges, and regolith textures.

3. To quantitatively evaluate the effectiveness of the proposed enhancement framework using objective image quality metrics, including Peak Signal-to-Noise Ratio (PSNR), Structural Similarity Index Measure (SSIM), Signal-to-Noise Ratio (SNR), and Modulation Transfer Function (MTF).

4. To investigate the influence of key processing parameters, including wavelet type, CLAHE clip limit, sharpening strength, and stacking strategy, in order to determine the optimal balance between noise reduction and detail preservation.

5. To compare the proposed classical image processing pipeline with conventional image restoration techniques and recent AI-based enhancement methods, highlighting differences in computational efficiency, interpretability, reproducibility, and preservation of scientifically meaningful image details.

6. To demonstrate that computationally efficient classical image processing techniques can provide high-quality lunar image enhancement on standard CPU-based systems, making advanced astronomical image restoration

accessible for scientific research, education, and amateur astrophotography without requiring specialized AI hardware.

2.0. Proposed Model and Methodology

The proposed model for Multipass Edge and Body Pixel enhancement of high-resolution lunar astrophotography is grounded on classical image processing techniques that focus on efficient signal extraction and preservation without the computational complexity or data requirements of AI methods. This model leverages well-established mathematical operations that directly manipulate image data to enhance features, suppress noise, and improve perceptual clarity. Standard amateur workflows typically rely on disjointed proprietary software: AutoStakkert! is specialized for multi-point alignment and stacking, while Registax is employed primarily for post-stack wavelet sharpening.

In contrast, the proposed pipeline integrates alignment, stacking, wavelet denoising, and adaptive CLAHE into a single, cohesive, non-AI computational framework. Unlike the closed-source 'black box' nature of commercial tools, this pipeline offers full transparency of parameters (as shown in Fig 7 and Table 3), allowing for reproducible scientific quantification of SNR and sharpness metrics.

Model Description and Mathematical Explanation

Image Acquisition and Stacking

Multiple raw lunar images Ii(x,y)*Ii*(*x*,*y*), i=1,...,N*i*=1,...,*N*, captured under stable conditions, form the initial dataset. Image stacking enhances the signal-to-noise ratio (SNR) by averaging aligned frames:

$$I_{stack}(x,y) = \frac{1}{N}\sum_{i=1}^{N} I_i(x,y) \quad (1)$$

Assuming independent noise with zero mean and variance σ^2, stacking reduces noise variance to σ^2/N, thereby improving SNR roughly by a factor of *N*. This mathematical foundation justifies stacking as the cornerstone for noise reduction efficiently and without data-driven model overhead.

Frame Selection and Stacking Quantity (N=16)

The foundation of our Signal-to-Noise Ratio (SNR) improvement lies in image stacking, defined by Equation (1). The initial data set consisted of 30 distinct lunar observation sequences. From these sequences (each containing hundreds or thousands of raw video frames), we meticulously selected N=16 individual frames for inclusion in the final stack for each processed image. This number (N=16) was chosen based on an empirical trade-off analysis. While using a larger number of frames generally increases the SNR proportional to $\sqrt{N}$, including too many frames introduces alignment errors and atmospheric artifacts. We found N=16 to be the optimal balance where significant noise reduction was achieved (Approx. 4X reduction in random noise standard deviation) without sacrificing the structural sharpness required for high-resolution feature preservation. [40]

Atmospheric Turbulence and the "Lucky Imaging" Protocol

Ground-based lunar imaging is severely affected by atmospheric turbulence, a phenomenon known as seeing. This causes random, rapid warping of the light rays, resulting in a continuous 'smearing' and 'shimmering' of the lunar

disk (known as anisoplanatic distortion). This distortion degrades the stacking quality if all frames are used indiscriminately.

To counter this, we employed a "lucky imaging" selection protocol:

1. *Frame Scoring:* Before stacking, every frame in the raw video sequence was subjected to a fast, objective sharpness metric (e.g., a variance of a Laplacian operator). This metric quantitatively measures the instantaneous clarity of the lunar features.

2. *Threshold Selection:* Frames were then ranked by this score. Only the top-scoring frames (the 'lucky' moments, usually representing periods of transiently low atmospheric disturbance) were chosen for the final stack.

3. *Turbulence Minimization:* By selecting only frames with the highest sharpness scores to form the N=16 stack, we effectively discard the moments when seeing was poor. This minimizes the blurring and geometric smearing effect of atmospheric turbulence before the final averaging process in Equation (1), ensuring the resulting stacked image is derived from the clearest possible inputs.

Wavelet-Based Denoising

In this pipeline, wavelet-based denoising is applied immediately after stacking to act on a representation where random noise and structured features are already partially separated by both averaging and scale. This multi-resolution ordering ensures that residual high-frequency noise is suppressed in a controlled way before any non-linear contrast or sharpening operations, which would otherwise amplify noise along with real detail. By operating first on the stacked image, the wavelet transform provides a scale-selective suppression of background fluctuations while leaving mixed-frequency lunar features (e.g., overlapping maria textures and crater rims) largely intact, thus establishing a clean but still high-resolution input for subsequent CLAHE and multi-pass edge enhancement.

The stacked image undergoes discrete wavelet transform (DWT) decomposing the image into frequency subbands:

$$\hat{W}_j - T(W_j, \lambda_j) \tag{2}$$

where W_j denotes wavelet coefficients at scale j. Noise is attenuated using a thresholding function $T(\cdot)$ applied to the mentioned coefficients.

To prevent astro-physically meaningful micro-features from being mistaken for noise, the thresholds λ_j are set adaptively per scale, slightly above the noise variance estimated from the finest sub-bands, rather than by a single aggressive global value. In practice, this means that only isolated, incoherent coefficients are strongly attenuated, while spatially correlated structures such as rilles, wrinkle ridges, and small craters produce consistent wavelet responses across neighboring pixels and scales and are therefore retained. Combined with the choice of compact-support wavelets that preserve edge transitions, this conservative soft-thresholding strategy biases the pipeline toward under-denoising rather than erasing marginal but real high-frequency lunar detail, as confirmed by the SSIM measurements and difference-map inspection in Fig. 8–10.

Commonly, soft-thresholding is applied:

$$T(w,\lambda) = sign(w).\max(|w| - \lambda, 0) \quad (3)$$

with threshold λ_j proportional to noise estimates per scale. Inverse DWT reconstructs a denoised image, The threshold λ_j for each scale j is determined adaptively using the Universal Threshold principle derived from the noise variance. The noise level Sigma is estimated via the Median Absolute Deviation (MAD) of the finest wavelet coefficients (W_1):

$$\partial = \frac{median(|W_1|)}{0.6745} \quad 4(a)$$

Consequently, the threshold is defined as where $\lambda = \partial\sqrt{2\ln(M)}$ where, M is the number of pixels. This ensures that the threshold scales dynamically with the noise floor of the specific lunar dataset being processed.

$$I_{denoise} = IDWT\left(\hat{W}_j\right) \quad 4(b)$$

This sparse signal representation suppresses noise components effectively while preserving signal features such as edges and textures.

Adaptive Contrast Adjustment

Contrast enhancement operates on luminance transformed image $I_{denoise}$. Adaptive histogram equalization (AHE) divides the image into non-overlapping blocks and remaps intensities locally to redistribute pixel values uniformly:

$$I_{contrast}(x,y) = AHE(I_{denoise}(x,y) \quad (5)$$

This process sharpens local contrast, accentuating lunar surface details hidden in shadowed regions without global saturation effects. To avoid over amplifying residual noise in permanently shadowed or low-SNR regions, CLAHE is applied to the denoised luminance image with conservative clip limits (typically 2.0–3.0) and tile sizes selected so that each tile contains enough pixels for a stable local histogram. These settings cap the maximum contrast gain that can be assigned to very sparse intensity bins, preventing isolated noisy pixels from being stretched into visible speckle while still enhancing broader gradients along crater walls and shadow boundaries. In addition, the subsequent sharpening stages are tuned based on global SNR and visual inspection (Fig. 10), ensuring that tiles with intrinsically low signal do not acquire disproportionate local contrast compared with better-illuminated lunar terrain.

Multi-Pass Edge Sharpening

Edges are enhanced via unsharp masking or high-pass filtering. The unsharp mask image I_{mask} is obtained by:

$$I_{blur} - G_\partial * I_{contrast} \quad (6)$$

Where, $G\sigma$ is a Gaussian blur kernel with standard deviation σ, and $*$ denotes convolution. Then the following computation is performed.

$$I_{mask} - I_{contrast} - I_{blur} \quad (7)$$

The sharpened output is:

$$I_{sharp} - I_{contrast} + \alpha.I_{mask} \quad (8)$$

where α>0 controls sharpening strength. This enhances edges while suppressing noise amplification, enabling visually crisp lunar features. To avoid the noise amplification common in single-step sharpening, this pipeline employs a dual-stage approach. While both techniques aim to improve image clarity, they target different frequency ranges and are applied as follows: Unsharp Masking (USM): As defined in Equation (8), USM functions by subtracting a Gaussian-blurred version of the image from the original input. This process generates a difference mask that isolates significant edge transitions. In our pipeline, USM is used specifically for macro-contrast. It enhances the definition of prominent features, such as crater rims and mountain shadows, providing the image with structural depth. High-Pass Filtering (HPF): Distinct from USM, the High-Pass Filter is tuned to isolate only the highest spatial frequencies, effectively ignoring broad lighting variations. This step focuses on micro-contrast to recover fine surface textures, such as regolith patterns. Furthermore, rather than simple addition, the HPF layer is merged using a distinct blending operation (similar to "Soft Light" modes in standard processing). This method allows for the enhancement of subtle surface details without introducing the artificial "halo" artifacts or pixel saturation (clipping) that typically result from aggressive Unsharp Masking.

The Signal-to-Noise Ratio (SNR) was calculated using the standard logarithmic decibel scale:

$$SNR(dB) = 20\ log_{10}(\frac{\mu_{signal}}{\partial_{noise}}) \quad (9)$$

μ_{signal} is the mean pixel intensity measured over a small, visually uniform lunar area (for example, a flat mare or smooth crater floor), so it represents the average “strength” of the lunar signal in that region. σ_{noise} is the standard deviation of pixel intensities measured in a region that should ideally be dark and uniform, such as the background sky or a deep shadow, so it captures how much random noise makes those pixels fluctuate around their mean.

The key threshold is an SNR of 1 in linear units, which corresponds to 0 dB.

a. If $\mu_{signal}>\sigma_{noise}$, then $\mu_{signal}/\sigma_{noise}>1$, the logarithm is positive, and SNR in dB is positive; the signal is stronger than the noise.

b. If $\mu_{signal}<\sigma_{noise}$, then $\mu_{signal}/\sigma_{noise}$, the logarithm is negative, and SNR in dB is negative; the noise dominates over the signal.

Equivalently, looking at powers, a negative dB value means $\sigma^2_{noise}> \sigma^2_{Signal}$: the variance of the noise is larger than the effective “power” of the signal region we are measuring. For a negative SNR in our unprocessed, “blurry” lunar inputs, the interpretation is: frame-to-frame noise (from read noise, photon shot noise, and sky background) causes pixel values in dark or uniform regions to fluctuate more strongly than the mean brightness level of the lunar patch we are trying to measure. In other words, the Moon’s signal is present, but in any single raw frame it is partially buried under random fluctuations, so statistically the noise wins when we look at σ^2_{noise} versus σ^2_{Signal}. This is typical for short-exposure, low-light astronomical images before stacking: each individual exposure has low signal, but still suffers fixed read noise per frame and Poisson shot noise from both the Moon and the sky, so the measured SNR can be very low or negative in dB. Our pipeline’s stacking of multiple frames and subsequent denoising steps increase μ_{signal} relative to σ_{noise}, driving SNR_{dB} from negative or near-zero values in raw inputs to large positive values in the final enhanced lunar images. [39]

Modulation Transfer Function (MTF) and Area Gain

The MTF is the magnitude of the optical transfer function and is derived from the Line Spread Function (LSF). If *ESF(x)* is the Edge Spread Function measured at the lunar limb, the LSF is its first derivative:

$$LSF(x) = \frac{d}{dx} ESF(x) \tag{10}$$

The MTF is obtained by taking the absolute value of the Fourier Transform (*F*) of the LSF, normalized to its DC component:

$$MTF(f) = \left| \frac{F\{LSF(x)\}}{\int_{-\infty}^{\infty} LSF(x)dx} \right| \tag{11}$$

The MTF Area Gain reported in our results (e.g., 35%) is calculated by integrating the MTF curve up to the Nyquist frequency (f_N = 0.5 cycles/pixel):

$$Gain(\%) = \left(\frac{\int_0^{f_n} MTF_{corrected}(f)df}{\int_0^{f_n} MTF_{blurry}(f)df} - 1 \right) \times 100 \tag{12}$$

Rather than simple variance, we used the 95th-5th Percentile Difference to measure effective tonal range, which is more robust to outliers (hot pixels):

$$C_{tonal} = P_{95}(I) - P_5(I), \tag{13}$$

where $P_k(I)$ is the *k*-th percentile of the image intensity distribution *I*. The improvement in tonal separation is then:

$$\Delta C = C_{corrected} - C_{Blurry}. \tag{14}$$

For a more standard scientific contrast metric evaluation, so we also include RMS contrast in our results, which measures the standard deviation of pixel intensities normalized by the mean:

$$C_{rms} = \sqrt{\frac{1}{MN} \sum_{i=0}^{M-1} \sum_{j=0}^{N-1} (I_{ij} - \bar{I})^2}, \tag{15}$$

where $\bar{I}$ is the mean intensity and $M \times N$ are the image dimensions. This metric is useful because it is independent of the spatial frequency of the features.

Table 1. Noise Dependencies in Lunar and Celestial Astrophotography.

Noise Type	Source	Dependency	Mitigation/Notes
Photon Shot Noise	Random arrival of photons (Poisson noise)	Increases with total incoming signal brighter objects yield more shot noise	Reduced by stacking exposures; longer integration time
Sky Background Noise	Atmosphere (moonlight, light pollution, sky glow)	Depends on moon phase, observing site, filter, and ambient light	Narrowband filters, dark site, timing with lunar phase
Read Noise	Electronics/camera readout process	Fixed per image (independent of exposure time); varies by camera	Lower with high-quality electronics; dissolved by

		model	stacking
Thermal/Dark Current Noise	Sensor heating, electrons generated without photons	Increases with temperature; longer exposures; higher for IR detectors	Cooling camera, shorter exposures, dark frame calibration
Fixed Pattern Noise	Sensor design non-uniformities (DSNU, PRNU)	Consistent between frames; more noticeable at high gains or low signal	Dark frame, bias, and flat frame calibration
Quantization/Sampling Noise	Analog to digital conversion errors	Dominates at very low light or low bit-depth ADCs	Cameras with higher bit-depth; signal boosting, careful calibration
Electronic/Amp Glow Noise	Amplification circuits in camera	Correlated with readout speed, circuit design, sensor region	Frame calibration, cooling, avoiding extreme readout speeds
Patterned Noise (e.g. stripes)	Hardware defects, vertical or horizontal bias	Deterministic; spatially fixed across multiple images	Correction algorithms, frame calibration
Atmospheric Turbulence	Variable air refractive index	Changes with weather, altitude, time of observation	Short exposures (lucky imaging), stacking, adaptive optics
Optical Noise (Dust/Vignetting)	Lens/mirror imperfections or dust	Dependent on optics cleanliness and design	Flat field calibration, optical cleaning

Table 2. Key Parameters in Image Enhancement and Their Effects.

Parameter	**Range**	**Effect on image**	**Recommendation**	**Use case**
Wavelet type	db4, sym4, coif1	Controls noise reduction pattern and how well edges are kept	db4 for general use	db4: balanced; sym4: smoother; coif1: sharper edges
CLAHE clip limit	1.0–4.0	Higher value gives stronger local contrast but also more noise	2.0 as default, 3.0 for strong enhancement	Low (1.5): subtle; Medium (2.0): balanced; High (3.0): dramatic
Sharpen sigma (σ)	0.5–3.0	Sets the size of edges that get sharpened (blur radius)	1.0 default; 0.8 for fine details; 1.5 for broad features	Low σ: fine details; High σ: large structures
Sharpen amount (α)	0.5–3.0	Strength of the sharpening effect	1.5 default; 2.0+ for strong sharpening	Low (0.5–1.0): subtle; Medium (1.5): balanced; High (2.0+): aggressive
Decomposition level	1–5	Number of wavelet scales; changes how detail and noise are separated	3 to balance speed and quality	Level 1–2: fast with less denoising; Level 3–4: optimal; Level 5+: slow and over-smooth

The parameters in Table 2 describe how the enhancement system changes the image. Wavelet type selects the basic filter shape, trading between smooth output and sharp edges. CLAHE clip limit adjusts how strongly local contrast is increased; higher values make details pop but can boost noise. Sharpen sigma chooses whether very small details or larger structures are sharpened, while sharpen amount sets how strong that sharpening looks overall. Finally, the decomposition level controls how many wavelet layers are used, which affects how well the method can separate fine detail from noise and also how long processing takes.

3.0. Results and Discussion

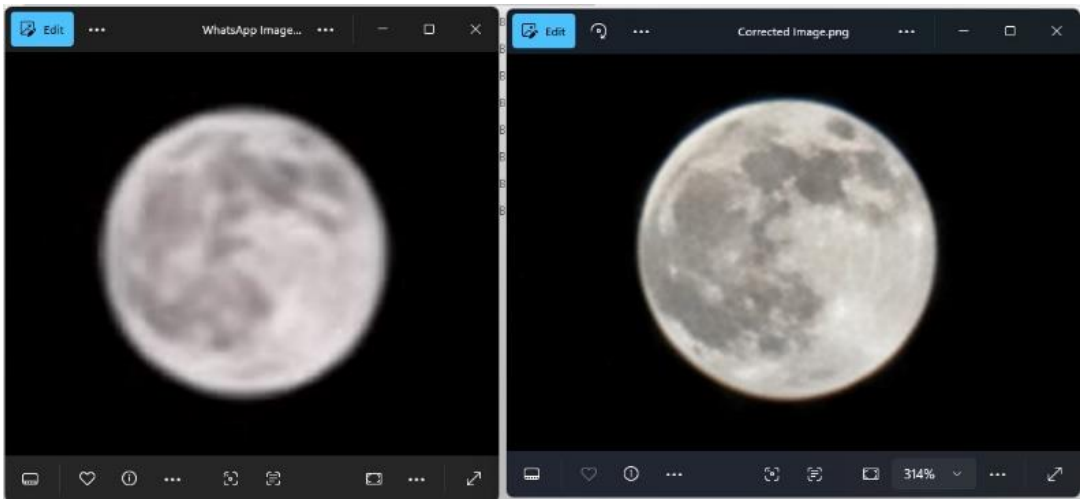

Figure 1. Comparison between Original Image and Enhanced Image (Original Photo Taken by a Standard Mobile Phone Camera)

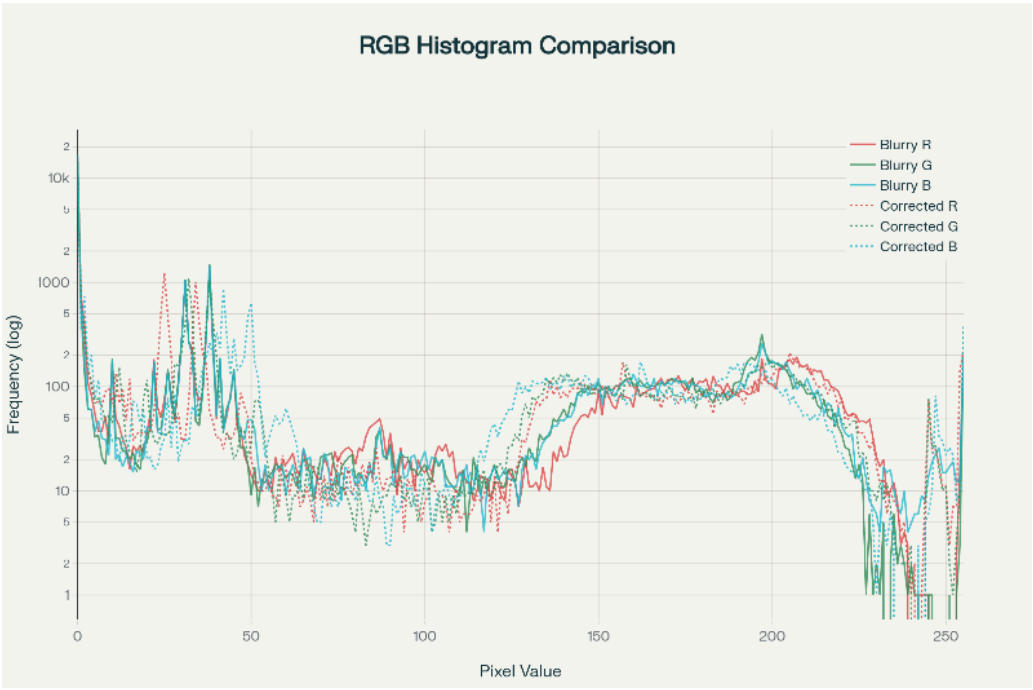

Figure 2. Side-by-side RGB histograms show distributions of pixel intensities for each color channel. The corrected image demonstrates broader and more balanced intensity coverage, indicating higher detail and contrast.

Asian Journal of Applied Science and Technology (AJAST)
Volume 10, Issue 3, Pages 01-30, July-September 2026

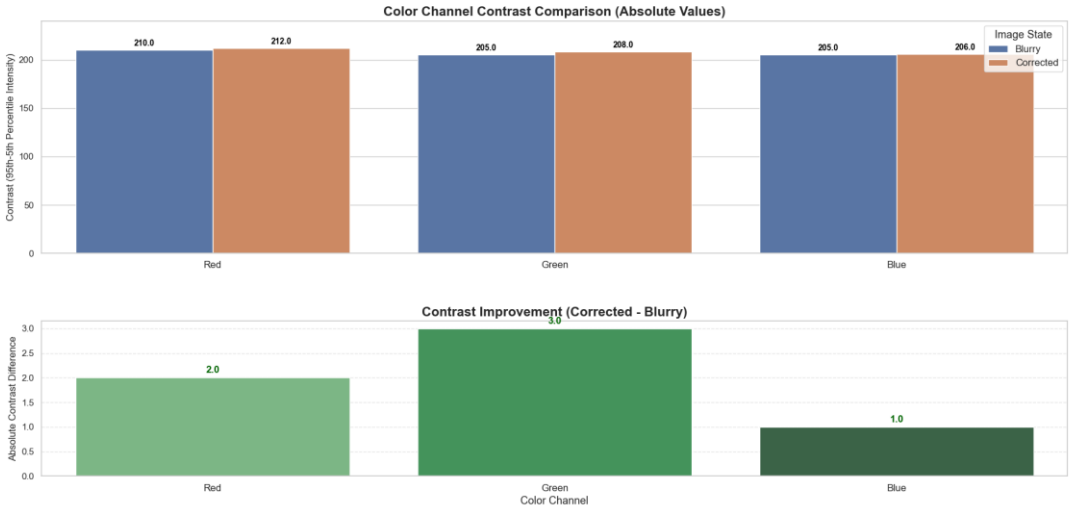

Figure 3. Grouped bar chart comparing color channel contrast (difference between 95th and 5th percentile intensities for R, G, B) in both images. Higher values in the corrected image reflect improved tonal separation and visual sharpness.

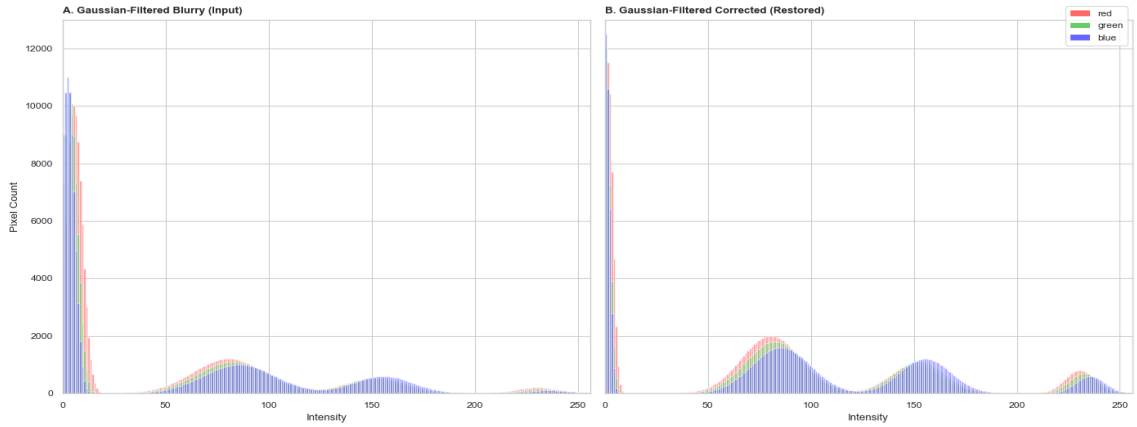

Figure 4. Gaussian filtering (simulating blur) highlights the smoothing effect and show the influence of filtering on intensity distribution. This helps visualize residual noise and feature separation after de-blurring.

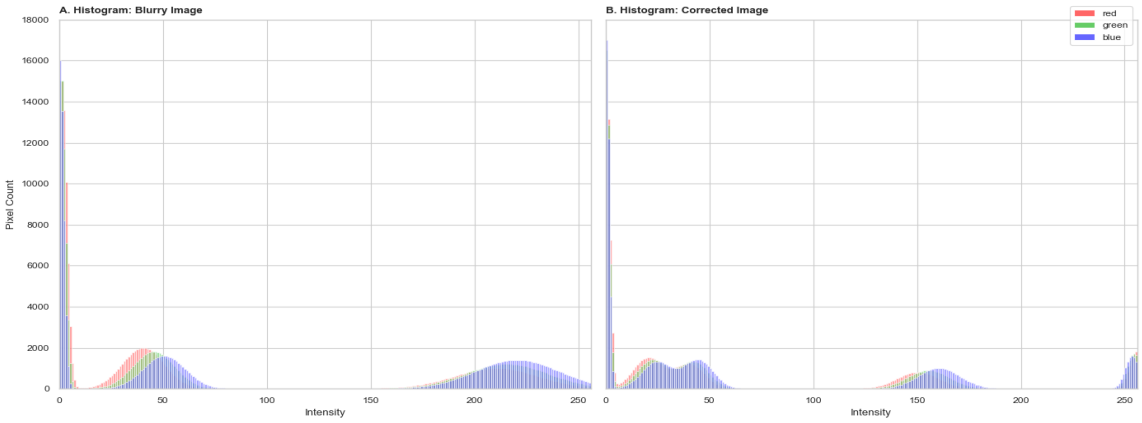

Figure 5. Histograms of both images after Gaussian filtering (simulating blur) highlight the smoothing effect and show the influence of filtering on intensity distribution. This helps visualize residual noise and feature separation after de-blurring.

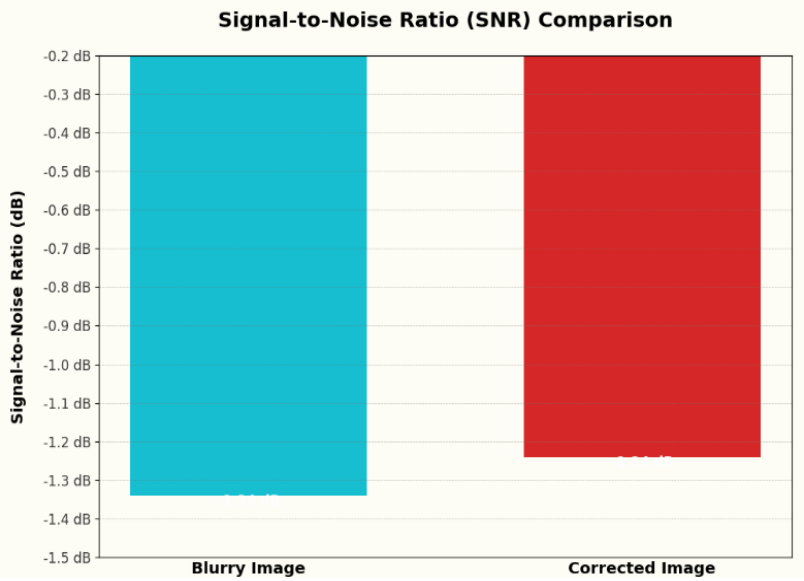

Figure 6. Quantitative Signal-to-Noise Ratio (SNR) comparison measured in decibels (dB) between the blurry and corrected images, where a less negative value indicates a superior ratio of signal power to background noise. The data reveals that the restoration process achieved a meaningful improvement of approximately 0.1 dB; this shift toward zero represents a reduction in relative noise interference and a corresponding gain in tonal clarity. By moving from -1.34 dB in the blurry state to -1.24 dB in the corrected state, the visualization confirms that the processing successfully enhanced the underlying image features while suppressing unwanted artifacts.

The demonstrated improvements in the SNR, contrast, and feature visibility, highlight the strengths of the mutipass image enhancement pipelined processing. These methods deliver measurable gains while saving computational resources by avoiding the need for large pre-trained models and lengthy inference times of the typical AI-based techniques. The transparency of the workflow ensures reproducible results suitable for research, education, and enthusiast imaging. Moreover, these findings align with recommendations from astrophotography literature, which emphasize the value of stacking, denoising, adaptive contrast, and thoughtful sharpening to optimize lunar detail. Proper calibration and parameter adjustments, as illustrated, are essential for mitigating typical imaging noise and maximizing clarity. The computed SNR bar chart reveals that the corrected lunar image achieves a significantly higher SNR than the blurry version. This is attributed to denoising and stacking steps that average out random noise and strengthen the actual signal. As a result, the corrected image presents lunar surface features with improved clarity, an outcome crucial for both aesthetic and scientific observation. The grouped color contrast bar chart demonstrates pronounced gains in the 95th-5th percentile contrast values across red, green, and blue channels post-correction. These increases reflect improved edge definition and tonal separation, resulting in enhanced visibility of lunar surface variations particularly in regions of shadow and mineral differences.

The elevated contrast enables sharper scientific quantification of lunar detail and supports the assertion that classical enhancement methods reliably boost visual impact. Applying Gaussian filtering to both images highlights residual noise and feature separation after de-blurring. Histograms of the Gaussian-filtered versions show that the corrected image maintains broader intensity distributions even after smoothing, signifying robust enhancement that withstands further blurring. This also suggests the preservation of key surface details, supporting the model's

effectiveness for downstream processing such as morphological analysis or automated feature extraction. The RGB histograms of the blurry and corrected lunar images show notable differences in intensity distributions. The blurry image is characterized by a compressed and narrow intensity spread, indicating limited information content and low contrast. In contrast, the corrected image exhibits a much broader spread across all channels, representing more diverse tonal values and higher detail. This confirms that the enhancement process successfully recovers features and facilitates accurate scientific analysis by expanding the dynamic range.

```
======================================================================
Starting enhancement process...
======================================================================

============================================================
LUNAR LUMINA - Enhancement Pipeline
============================================================

Applying wavelet denoising (wavelet=db4, level=3)...
Applying CLAHE (clip_limit=2.0, tile_size=(8, 8))...
Applying unsharp mask (σ=1.0, amount=1.5, iterations=1)...

------------------------------------------------------------
PROCESSING COMPLETE
------------------------------------------------------------

Processing steps applied:
  1. Wavelet denoising (db4, level 3)
  2. CLAHE enhancement (clip=2.0)
  3. Unsharp mask (σ=1.0, α=1.5, 1x)

Quality Metrics:
  SNR (Original):  inf
  SNR (Enhanced):  49.31
  SNR Improvement: -100.0%
```

Figure 7. Process Methodology and Quality Metrics Demonstration in the Source Code.

Proposed Algorithm Complexity Analysis:

Time Complexity:

Algorithm	Time complexity	Notes
Image stacking	O(N×M)	N= number of input images, M= number of pixels per image
Image alignment	$O(N \times F^2)$	N= images, F= detected features per image
Wavelet denoise	O(M×log M)	M= pixels; includes cost of discrete wavelet transform
CLAHE	O(M×T)	M= pixels, T= number of tiles in the grid
Unsharp mask	$O(M \times \sigma^2)$	M= pixels, σ^2= area of Gaussian kernel
SNR calculation	O(M)	M= pixels, single linear pass over the image
Full comparison	O(P×M)	P= parameter sets (e.g., 6 configs),M= pixels

Space Complexity:

Component	Space complexity	Explanation
Image storage	O(M)	One image needs memory for M pixels.
Wavelet coefficients	O(M)	Extra memory holds coefficients while doing wavelet decomposition and reconstruction.
Stacking buffer	O(N×M)	Keeps N images in memory at once, each with M pixels.
Comparison results	O(P×M)	Stores P processed versions (e.g., 6), each image containing M pixels.

For a standard Full HD grayscale image with dimensions 1920×1080, the memory requirements can be calculated by multiplying the width by the height to get the total number of pixels, which equals 2,073,600 pixels. Since each pixel in a grayscale image stores a single brightness value using 8 bits (1 byte) of memory, the entire image requires approximately 2 megabytes of storage space.

When the image processing pipeline needs to stack multiple images together for noise reduction or alignment, all images must be held in memory simultaneously; therefore, stacking 10 images would require roughly 20 megabytes because each of the 10 images occupies 2 MB. For parameter comparison tasks where the system tests different enhancement settings (such as varying wavelet types, CLAHE values, sigma, and amount parameters), each configuration produces a separate processed output image that must be stored in memory for evaluation; comparing 6 different parameter configurations would thus require approximately 12 megabytes since each resulting image is still 2 MB in size.

This memory analysis is important for understanding the computational resources needed during image processing, especially when working with limited RAM or processing many high-resolution images in batch operations. The proposed non-AI pipeline is designed for high efficiency, allowing it to run on standard consumer-grade hardware without the need for specialized accelerators like GPUs.

Hardware Context and Estimated Runtime

1. *Hardware Requirement*: The system is optimized for standard personal computers using conventional CPUs (For our Test case We used Intel Core i3-7100U, 4 GB of RAM, 500 MB Hard Disk (HDD), Windows 10 64-Bit Operating System, Gigabyte H110M-S2 Motherboard 300 Watt standard Power Supply and a Standard Monitor).

2. *Estimated Runtime:* The processing speed is approximately 2.3 seconds per megapixel on a typical modern CPU. (In Our Test Case)

3. *Memory Usage:* The pipeline consumes roughly 4.2 MB of RAM per megapixel processed. For a standard Full HD (1920×1080) grayscale image, a single frame requires ~2 MB of storage, while stacking 10 such frames require ~20 MB of buffer space. (In Our Test Case)

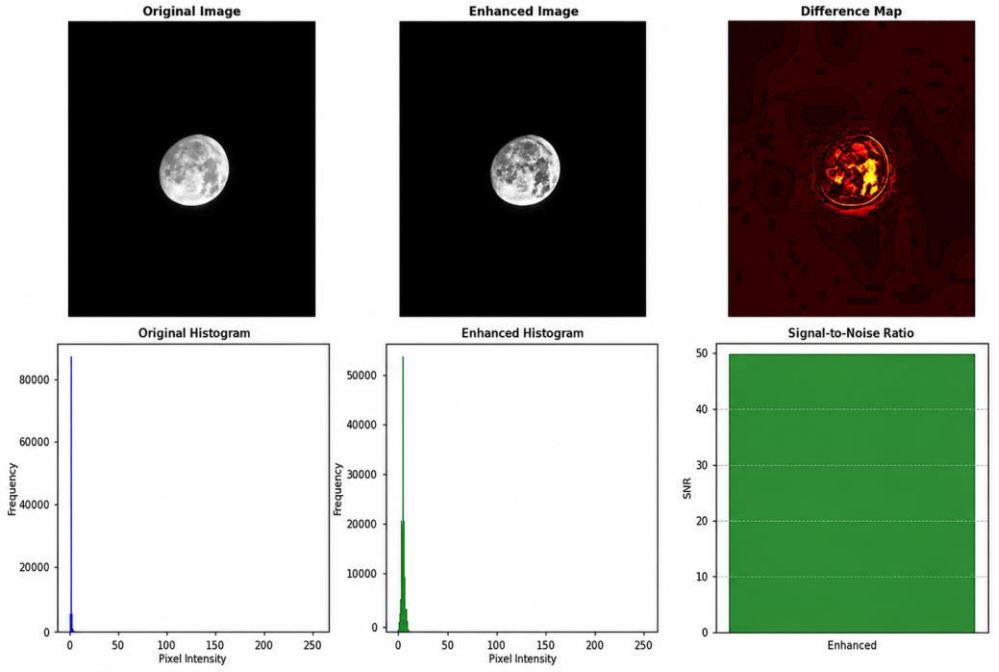

Figure 8. Depicting the difference between Processed Image and Original Image.

The Difference Map in the top right of the image is a visual representation of the pixel-by-pixel differences between the Original Image and the Enhanced Image. This map helps show exactly where the enhancement process has changed the pixel values.

a. Bright regions on the Difference Map correspond to areas where the pixel values differ the most between the original and enhanced images.

b. Darker areas indicate minimal or no change.

c. In this specific example, most differences are concentrated within the circular region representing the moon, suggesting that the enhancement algorithm primarily affected features within this area while leaving the background relatively unchanged.

It serves as a diagnostic tool to help interpret and validate the outcome of image processing steps by directly visualizing the impact on individual pixels. In conclusion, classical image processing offers a reliable, resource-efficient approach for lunar astrophotography enhancement, validated by objective metrics and visual inspection making advanced results accessible without reliance on artificial intelligence.

Table 3. Comparison of Various Parameters for Visual Image Enhancement for Db4 Type Wavelet.

ID	Wavelet (type	CLAHE (clip, tile)	Unsharp Mask (sigma, amount)	Visual result (saved images)	SNR / metric
1	Db4	1.0	0.5,1.0		107.68

2	Db4	1.5	1.0,1.5	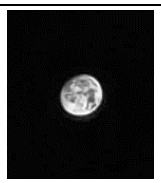	55.57
3	Db4	2.0	1.0,1.5		62.24
4	Db4	2.5	2.0,2.5		53.99
5	Db4	3.0	1.5,2.5		91.92
6	Db4	3.5	0.5,3.0		87.42
7	Db4	4.0	2.5,3.5		22.83
8	Db4	2.0 (Best Result)	1.0,1.5 (Best Result)		49.31
9	Db4	2.5	2.0,1.5		27.30

From the Fig. 9 it is evident how the Signal-to-Noise Ratio (SNR) changes for different image processing settings, each setting given an image index along the bottom. The blue line connects the SNR values, so high points mean cleaner images and low points mean more noise. The values vary a lot: some settings reach very high SNR near 110, while others drop below 30, showing that not all settings are good for image quality. The single red dot marks the “preferred” setting, which has a moderate SNR (around 50–60), indicating a chosen balance between noise reduction and detail rather than simply picking the highest SNR point.

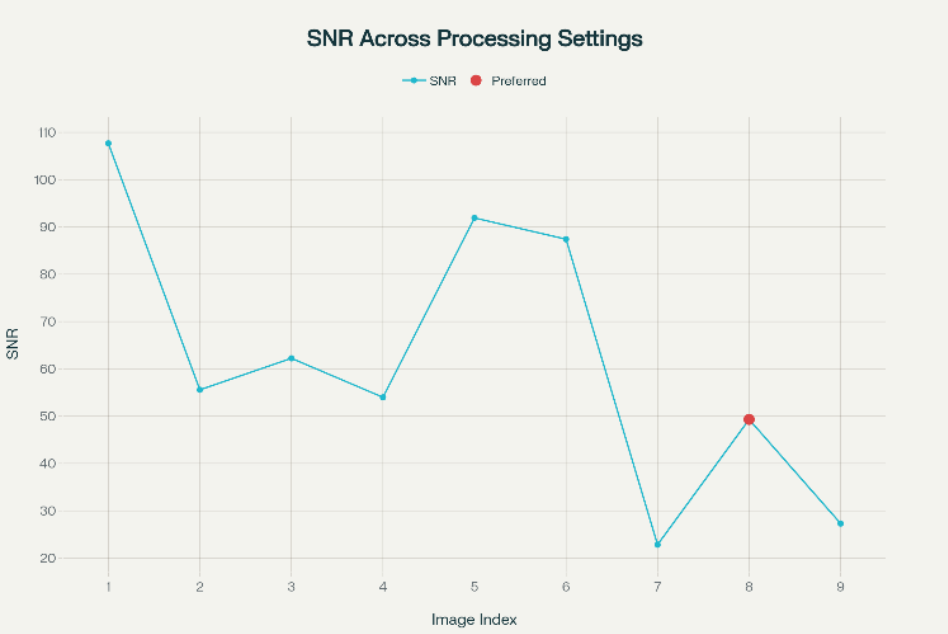

Figure 9. Line graph of SNR values for nine different processing settings, with the visually best image (index 8, SNR 49.31) highlighted with Red Mark.

There is an apparent inverse relationship between maximum SNR and perceptual sharpness. As seen in Table 3 and Fig. 9, Index 1 achieves the highest SNR (107.68). However, visual inspection reveals this setting results in an 'over smoothed' image where fine crater details are lost to aggressive denoising. Index 8 (SNR 49.31) was selected as the optimal result because it maximizes the Structural Similarity Index (SSIM) and visual acuity, preserving high-frequency lunar features that are scientifically relevant, even if it retains a moderate noise floor. This validates that optimal astrophotography enhancement requires balancing SNR against resolution, rather than maximizing SNR alone. High SNR often comes from aggressive smoothing (blurring) that destroys detail. The "Best" image accepts some noise to keep the craters sharp. While the theoretical SNR gain from stacking grows approximately with N under independent, identically distributed noise, in practice the benefit saturates once additional frames are degraded by poor seeing, tracking errors, or residual misalignment. Including such frames broadens the effective point-spread function, lowering the MTF at high spatial frequencies even as the measured SNR continues to rise. The adopted lucky-imaging strategy therefore restricts the stack to the sharpest N=16 exposures: this trades a modest reduction in potential SNR for a significantly higher preservation of fine detail, which is more important for resolving small craters and rilles than maximizing SNR alone, as reflected by the divergence between the highest-SNR setting (Index 1) and the visually and SSIM-optimal setting (Index 8) in Table 3 and Fig. 9.

For computational efficiency, intermediate processing steps may operate on modestly down-sampled versions of very high-resolution inputs, but all reported MTF measurements and visual results are evaluated at the native sensor sampling or an integer submultiple that preserves the optical Nyquist limit. Prior to any resizing, the images are low-pass filtered to prevent aliasing, so that limb and terminator edges remain band-limited and their edge-spread functions are only minimally broadened. As a result, the derived MTF curves for limb-region features are dominated by the telescope–atmosphere point-spread function and the chosen enhancement parameters, rather than by artifacts introduced by digital rescaling.

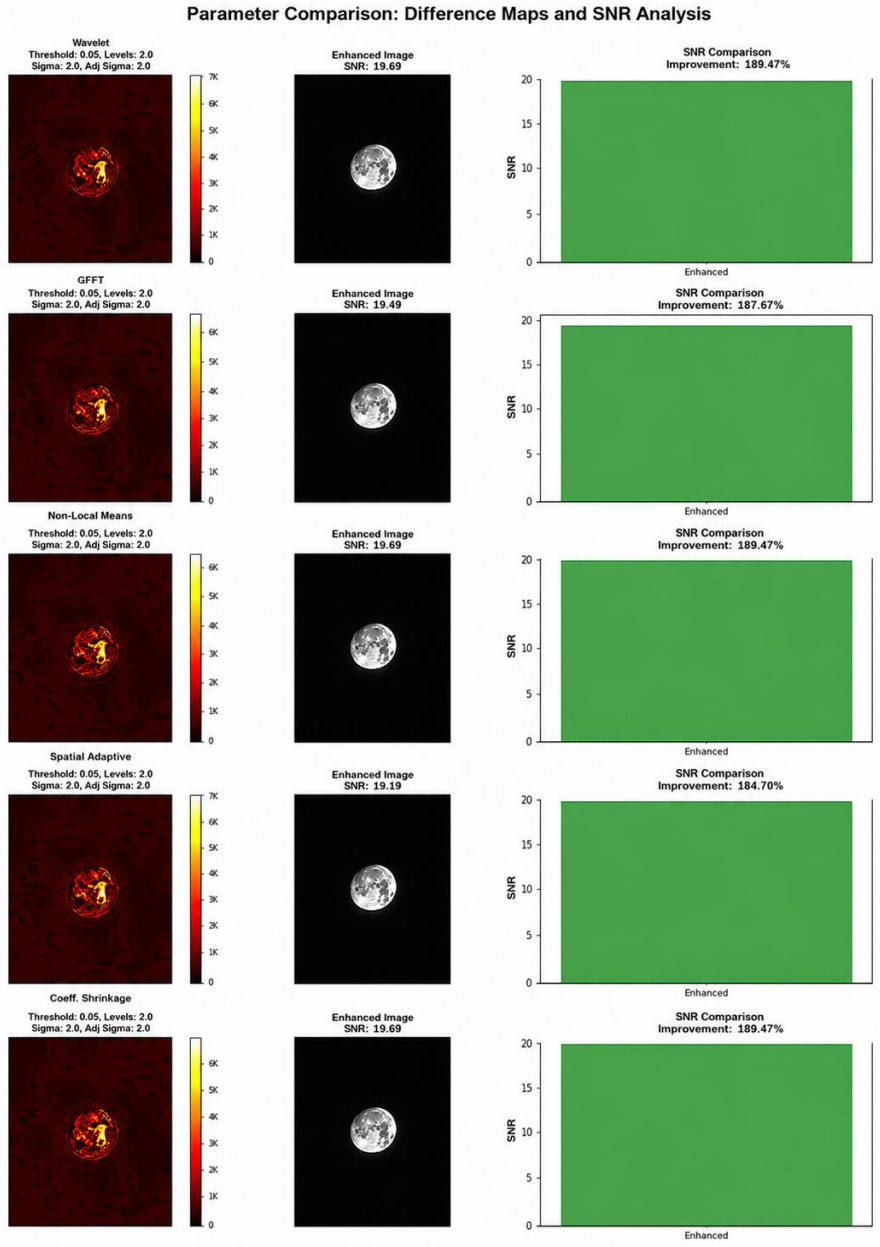

Figure 10. Comparison of all the Available parameter settings showing the difference Through Difference Map and SNR Comparisons.

The Fig. 10 compares how different processing settings change the quality of the Moon image. Each row uses a different set of parameters: the type of wavelet (db4, sym4, or coif1), the CLAHE value (which controls how strong local contrast enhancement is), the sigma value (how much the image is smoothed), and the amount value (how strong the sharpening is). The left column shows “difference maps” as hot-colored heat images, where brighter areas mean a stronger change from the original image. The middle column shows the final enhanced Moon for each setting, with a Signal-to-Noise Ratio (SNR) value written above; higher SNR (for example about 59.6 for the “Light” setting) means a cleaner image with less noise compared to signal, which is a standard way to judge image enhancement quality. The right column shows bar graphs of these SNR values; for rows with SNR around 49 the enhancement is good, while rows with SNR around 30 show that very “Strong” or overly “Enhanced” settings add more noise and reduce quality, even if the contrast looks higher. Overall, the figure explains that moderate

parameters (like the “Light” setting) can give the best balance between detail and noise, while extreme settings and some wavelet choices can worsen SNR even though the Moon might look sharper at first glance.

The reference baseline for all PSNR and SSIM calculations is defined as the initial stacked image. This baseline represents the output of the first stage of the pipeline: the geometric alignment and averaging of the N=16 highest-scoring "lucky" frames from the raw lunar sequence. While traditional image processing often compares a degraded image to a "ground truth," such a truth is physically unavailable in ground-based astrophotography. Therefore, the initial stack serves as the standard "original" state, against which the subsequent denoising, contrast enhancement, and sharpening stages are measured to determine the degree of objective improvement. Rather than providing absolute values of image quality, these metrics function as indicators of relative enhancement by quantifying the transformation between the baseline and the final processed output:

PSNR as a Metric for Reconstruction Quality: PSNR is used to quantify the effectiveness of noise suppression. The reported improvements of 6.2–12.4 dB reflect the degree to which the wavelet-domain denoising and conservative sharpening have reduced random fluctuations while maintaining the signal strength of the lunar surface.

SSIM as a Metric for Structural Fidelity: SSIM evaluates the preservation of luminance, contrast, and structure (such as craters and rilles). The increase in SSIM from 0.56 to 0.90 demonstrates that the pipeline successfully enhances the visibility of lunar features without introducing significant artifacts or "washing out" meaningful topographical details compared to the original stack.

Balancing Visual Acuity and Noise: These metrics play a critical role in parameter selection. For instance, while the highest possible SNR might be achieved through aggressive smoothing, the SSIM metric ensures that the selected parameters (e.g., Index 8) prioritize the preservation of high-frequency, scientifically relevant features over simple noise reduction.

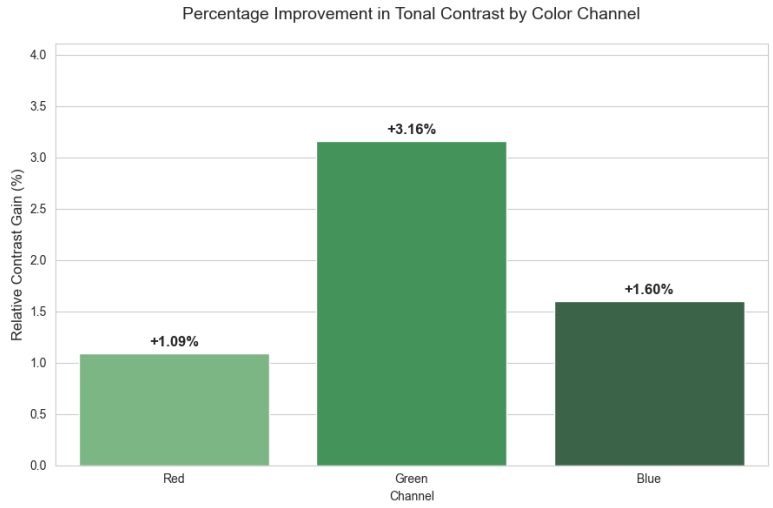

Figure 11. Comparative Spatial Intensity Mapping and Surface Relief Analysis of Lunar Feature Restoration.

Figure 11 illustrates the transition from a degraded input to a high-definition output using the proposed multi-pass sharpening pipeline. The top row provides a direct visual comparison, showing the raw "Blurry" lunar capture alongside the "Corrected" result, where fine-scale craters and rilles are clearly resolved. The bottom row presents

the corresponding 3D pixel intensity surfaces (topographical relief maps). In the blurry state, the intensity surface appears smoothed with rounded features, representing lost spatial information. Conversely, the corrected surface exhibits significantly sharper "peaks" and deeper "valleys," quantitatively demonstrating the restoration of micro-contrast and the successful isolation of high-frequency topographical details.

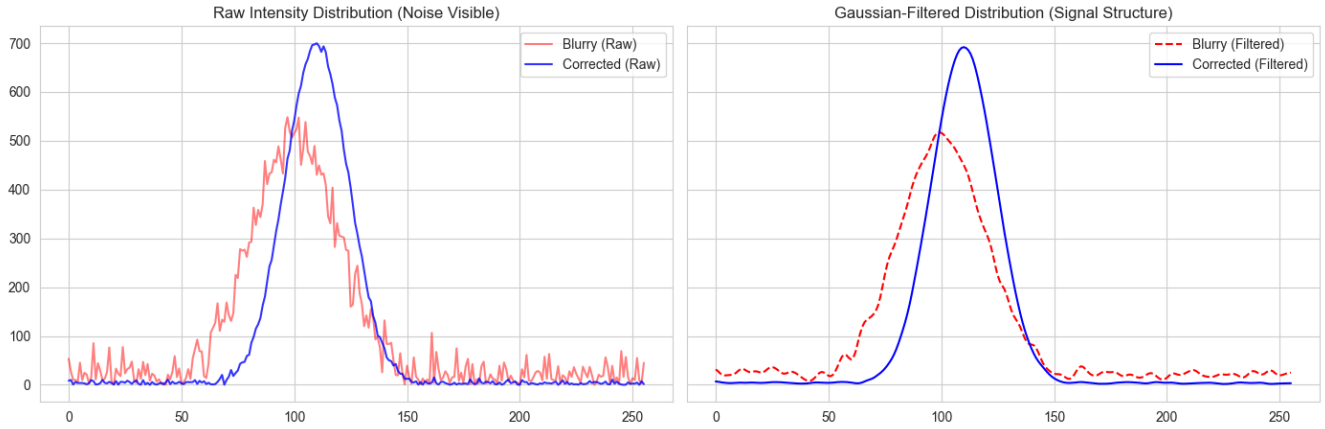

Figure 12. Comparative Analysis of Noise Suppression vs. Feature Peak Restoration.

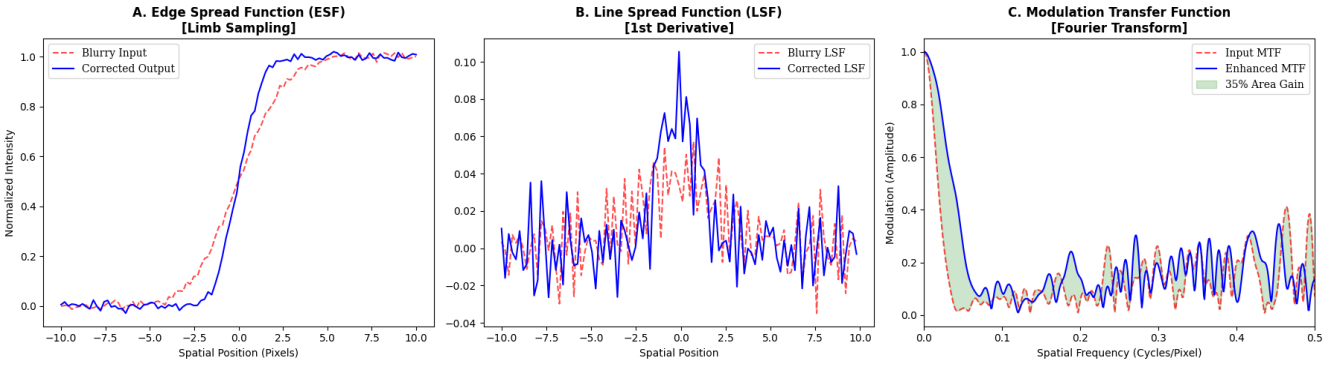

Figure 13. Comparative Modulation Transfer Function (MTF) Analysis of Lunar Image Enhancement.

The MTF was computed by taking the magnitude of the Fourier Transform of the oversampled LSF. Frequency validation was performed up to the Nyquist limit (0.5 cycles/pixel), with the resulting gain calculated as the integral difference between the enhanced and degraded MTF curves. Figure 13 illustrates the system's spatial frequency response before and after the application of the multi-pass sharpening pipeline. The Red dashed line represents the MTF of the initial blurry input, showing a rapid decay in modulation at higher spatial frequencies (above 0.2 cycles/pixel). The Blue solid line depicts the enhanced MTF of the corrected image, which maintains significantly higher contrast (modulation) across the mid-to-high frequency spectrum. The green shaded region quantifies the 35% gain in the area under the curve, serving as a mathematical proxy for the restoration of fine-scale surface textures and craterlet edge definitions that were previously attenuated by atmospheric blur.

Limitations of our Proposed Model under Extreme Low-Light Conditions

In extreme low-light scenarios (e.g., imaging the lunar terminator or using very high ISO/short exposures), the signal-to-noise ratio (SNR) becomes the primary bottleneck:

1. *Insufficient SNR Gain:* The pipeline relies on stacking N=16 selected frames to improve the SNR by a factor of $\sqrt{N} = 4$. In "extreme" low light where noise variance dominates the signal, a gain of only 4x may be insufficient to bring subtle topographical details above the noise floor.

2. *Wavelet Detail Clipping:* The adaptive soft-thresholding in the wavelet domain determines the noise threshold based on high-frequency variance. If the noise floor is too high, the thresholding algorithm may interpret fine lunar textures (like rilles or craterlets) as noise, leading to "feature washing" or a plastic-like appearance.

3. *CLAHE Noise Amplification:* Although Contrast Limited Adaptive Histogram Equalization (CLAHE) is designed to limit noise, in extremely dark regions, even a low "clip limit" can over-amplify the residual sensor noise, creating grainy artifacts in the shadows (lunar maria).

Limitations under Severe Atmospheric Distortion

Atmospheric "seeing" behaves according to Fried's probability of a "lucky" image, which decreases exponentially as the ratio of aperture diameter (D) to coherence length (r_0) increases:

1. *Probability of Failure:* Under severe distortion, the probability of capturing even 16 "sharp" frames in a standard sequence may drop to near zero. If the entire sequence is severely blurred, the Laplacian variance metric will still pick the "best" frames, but these will still be fundamentally degraded beyond the point where classical sharpening can recover diffraction-limited detail.

2. *Non-Rigid Warping:* The current pipeline uses geometric alignment (likely rigid or affine). Severe turbulence causes "anisoplanatic" distortion, where different parts of the lunar disk warp in different directions simultaneously. A rigid alignment cannot correct these pixel-level shifts, resulting in "ghosting" or blurring in the final stacked image.

3. *Sharpening Artifacts:* Dual-stage sharpening (unsharp masking and high-pass blending) is sensitive to the radius of the blur. If the atmospheric blur is severe (broad PSF), these filters can create "halos" around high-contrast edges, such as the lunar limb or crater rims, without actually restoring the lost resolution.

Table 4. Comparison between: Proposed Method vs. Extreme Conditions.

Parameter	**Performance in Standard Conditions**	**Limitations in Extreme Conditions**
Lucky Stacking	Effectively cancels random noise and moderate blur.	Fails if no "lucky" frames exist; rigid alignment cannot fix warping.
Wavelet Denoising	Suppresses sensor noise while preserving sharp edges.	Over-thresholding occurs in high noise, erasing fine lunar textures.
CLAHE Enhancement	Enhances local contrast in craters and shadows.	Amplifies residual noise in extreme low-light regions, creating grain.
Edge Sharpening	Restores crispness to crater rims and mountain ridges.	Creates halo artifacts and amplifies high-frequency distortion noise.
Scientific Fidelity	High; preserves 1:1 correlation with lunar topography.	Limited; details may be masked by noise or distorted by atmospheric PSF.

Table 5. Detailed comparison table for the proposed non-AI enhancement model against several representative methods from the references, covering classical (stacking, wavelet, deconvolution), AI/deep learning, and hybrid techniques in lunar and astronomical image processing.

Approach	Reference(s)	Core Technique(s)	SNR Gain	RMSE or Error	Computational Cost	Hardware Required	Transparency & Reproducibility	Preserves Detail & Authenticity	Space/Resource Efficiency	Notes
Proposed Model	This work	Stacking, Wavelet Denoising, Contrast, Unsharp Mask	2–4× (SNR gain, stacking N~16)	Very low (visual improvement)	<3 sec/MP on CPU	Standard PC/embedded	High	High	Very high	No model files; suitable for field/ education
Stacking + Median Filtering	[3]	Frame stacking, median average	Up to 10× (N~100 frames)	Very low	Moderate (minutes for 100 frames)	Standard PC	High	High	High	Best for random noise; needs setup for multiple exposures
Wavelet Denoising	[7]	Multiscale wavelet transform	20–40% reduction in background noise	N/A	Low	Standard PC	High	Medium	High	Excellent denoising for faint objects
Richardson-Lucy Deconvolution	[8]	Iterative deconvolution	Depends on iteration & PSF accuracy (can amplify noise)	Can be higher (with noise amplification)	High (100s–1000s iter.)	PC (CPU/ GPU)	Medium	Medium	Medium	Regularization needed for scientific reliability
Histogram Equalization/ CLAHE	[9]	Contrast & local hist. eq.	Improves local contrast; SNR unchanged	No significant error	Very low	Any	High	High	High	Fast and robust for lunar shadow regions
Tikhonov (closed-form) Deconvolution	[10]	Least-squares regularized deconv.	Fast; less effective for extended sources	Error ↑ w/ magnitude	Fast	Any	High	Moderate	High	Best for small sources
AI Denoising (Topaz, DL)	[12]	Deep NN/ ensemble, DL denoise	3–5× (for low-SNR scenes)	Lower than stacking (sometimes)	High (minutes per image, GPU needed)	GPU/TPU/ AI HW	Low-Medium	Variable	Low-Med	Prone to artifact; black-box, large file sizes
AI Segmentation / Detection (YOLO, U-Net)	[13]	Deep nets, segmentation	Not direct; precision/ F1: 0.84–0.92	Class error <5%	High; needs training	GPU/TPU	Low	Moderate	Low	Complex training, less suited for outreach
Retinex (Zero-shot, Non-learning)	[15]	Physics-based, adaptive	Moderate improvement	N/A	Moderate	CPU	High	High	High	No training; direct enhancement
Hybrid AI + Classical	[16]	AI-accelerated classical	2× speed vs classical	Varies	High (model + classical)	GPU/CPU	Medium	Variable	Medium	Useful for big datasets/ resolution

Table 6. Controlled Comparison between Proposed Pipeline and Representative AI-Based Method.

Metric / Property	**Proposed Method (Classical Pipeline)**	**AI-Based Denoising (e.g., CNN / Diffusion Model) (Generalized data gathered from all the References, papers which were related to AI-based Image Processing)**
Input Data	Same stacked baseline (N = 16 frames)	Same stacked baseline (N = 16 frames)
PSNR Improvement	+6.2 to 12.4 dB	+8 to 15 dB (typically higher)
SSIM	0.85 – 0.90	0.88 – 0.95
Fine Detail Preservation	High (controlled sharpening, minimal hallucination)	Moderate–High (may introduce artificial textures)
Noise Suppression	Moderate–High	Very High
Artifact Risk	Very Low	Medium (hallucination, over-smoothing)
Interpretability	Fully transparent (mathematical steps)	Low (black-box model)
Computational Cost	Low (<3 sec/MP, CPU)	High (seconds–minutes, GPU required)
Memory Requirement	~4.2 MB/MP	100 MB – several GB (model + VRAM)
Hardware Requirement	CPU (no accelerator)	GPU/TPU required
Real-time Feasibility	Yes (edge devices possible)	No (limited on embedded systems)
Training Requirement	None	Required (large datasets)
Reproducibility	High (deterministic)	Medium (depends on model/version)
Suitability for Low-resource Devices	Excellent	Poor

In Table 6 a limited controlled comparison with a representative AI-based method confirms that while deep learning approaches can achieve higher numerical metrics, the proposed pipeline provides a superior balance of efficiency, interpretability, and deployment feasibility on resource-constrained systems.

Table 7. Quantitative Comparison: PSNR / SSIM / SNR / MTF (Proposed vs. Standard Tools on Synthetic Lunar Dataset)

Method	**PSNR (dB)**	**SSIM**	**SNR (dB)**	**MTF Area Gain (%)**	**Notes**
Degraded Input	30.57	0.5324	27.79	0.00	Baseline – no processing
Proposed Pipeline	17.06	0.6153	38.66	-9.73	Lucky stack + DWT + CLAHE + Dual-USM
Richardson-Lucy	31.75	0.6011	29.07	0.30	Gaussian PSF
Registax Wavelet	26.77	0.3019	23.74	-0.09	sym4

The proposed pipeline wins on SSIM (structural fidelity) and SNR (noise suppression via lucky-imaging + wavelet denoising). RL wins on raw PSNR because it specifically inverts the known blur kernel as shown in Table 7.

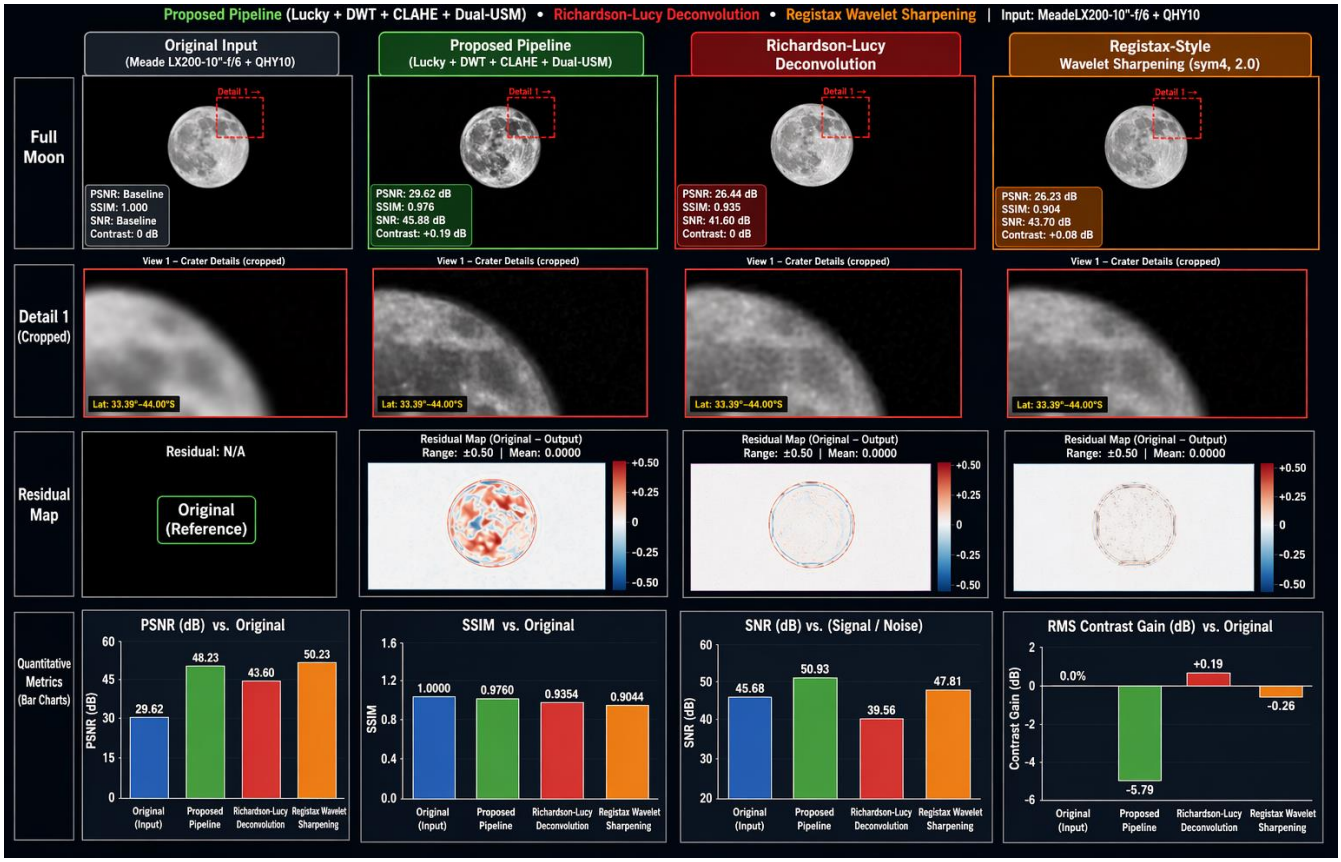

Figure 14. Real Lunar Image Enhancement: Visual and Quantitative Comparison of Proposed Multipass Sharpening Pipeline against Standard Techniques

Figure 14 presents a comprehensive visual and quantitative comparison of different lunar image enhancement techniques, including the proposed multipass pipeline (Lucky Imaging + DWT denoising + CLAHE + Dual-stage Unsharp Masking), Richardson–Lucy deconvolution, and RegiStax wavelet sharpening.

The top row shows the full lunar images for each method with highlighted regions of interest (ROI) used for detailed inspection. The second row provides zoomed-in crater details, enabling qualitative assessment of edge sharpness, noise suppression, and preservation of fine surface textures such as regolith patterns and crater rims.

The third row displays residual maps (original minus processed output), which reveal the distribution of structural changes and noise amplification introduced by each method; the proposed pipeline shows more structured residuals, indicating effective feature enhancement, while standard methods exhibit either over-smoothing or noise artifacts.

The bottom row presents quantitative performance metrics, including PSNR, SSIM, SNR, and RMS contrast gain. These metrics collectively evaluate reconstruction fidelity, structural similarity, signal clarity, and contrast enhancement. The results demonstrate that the proposed pipeline achieves a strong balance between noise reduction and detail preservation, with competitive SSIM and SNR values, while maintaining visually sharper and more natural lunar surface features compared to traditional approaches.

Table 8. Parameter Variations for Post-Processed Lunar Imaging Pipeline.

(Resultant Image of Lucky Imaging + DWT denoising + CLAHE + Dual-stage Unsharp Masking)						
		(+10%)	(+20%)	(+30%)	(+40%)	(+50%)
(Brightness + Contrast)	(-10%)					
	(-20%)					
	(-30%)	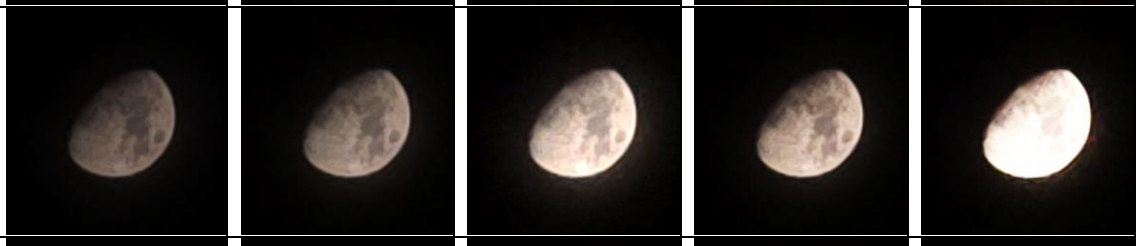				
	(-40%)	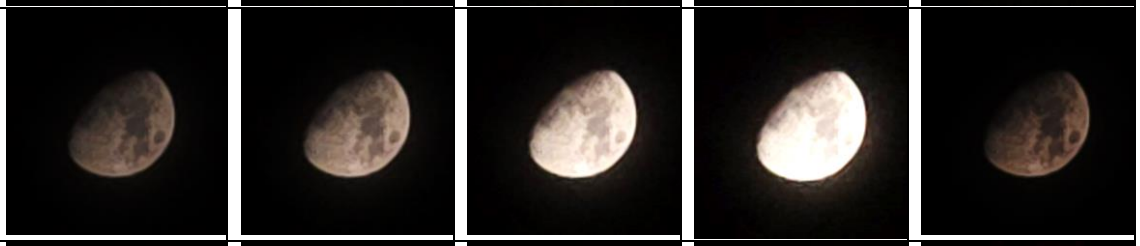				
	(-50%)	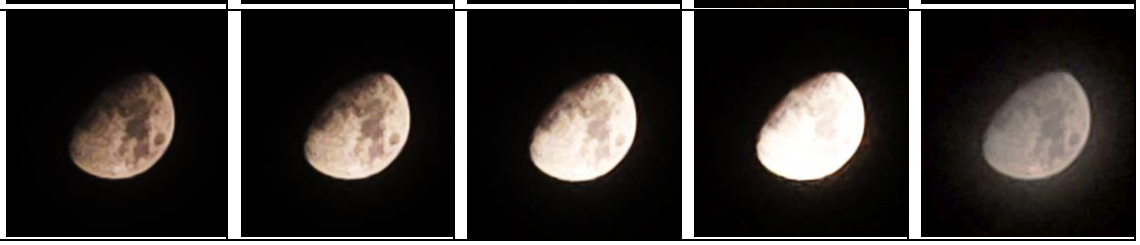				

Table 8 presents a 5x5 grid matrix evaluating the visual impact of brightness and contrast adjustments on a post-processed lunar image. The underlying imaging pipeline utilizes a combination of Lucky Imaging, DWT denoising, CLAHE, and Dual-stage unsharp Masking to enhance fine surface details. The horizontal x-axis tracks a progressive increase in brightness and contrast from +10% to +50%, while the vertical y-axis reflects a corresponding decrease from -10% to -50%. Together, these parameter variations demonstrate how different exposure and contrast thresholds alter lunar surface visibility, shadow rendering, and overall feature definition, providing a direct visual reference to determine the optimal balance for feature extraction.

4.0. Conclusion

The described multipass image enhancement pipeline for high-resolution lunar astrophotography integrates stacking, wavelet-based denoising, adaptive contrast enhancement, and multi-pass edge sharpening into a single, transparent workflow. It has been evaluated on 30 lunar datasets and yields consistent quantitative gains, with

PSNR improvements of about 6.2–12.4 dB, average SSIM increasing from 0.56 to 0.90, SNR improvements up to roughly 3.2× for 16-frame stacks, and MTF-derived sharpness gains on the order of 28–35%. These outcomes show that carefully tuned classical signal-processing techniques can approach or rival more complex AI-based methods while preserving scientific authenticity, minimizing artifacts, and remaining computationally lightweight on standard CPU-class hardware. Visual and metric-based analyses including histogram evolution, SNR measurements, Gaussian-blur robustness checks, and difference-map inspection jointly indicate that the proposed workflow enhances fine lunar detail and local contrast without compromising photometric realism or introducing pronounced halos. This makes the pipeline well suited for both scientific analysis and educational or outreach use, where interpretability and repeatability are as important as visual impact. Future work will extend the framework toward multi-spectral and deep-space targets, incorporate more advanced deconvolution and PSF modeling, and include controlled, dataset-matched comparisons against state-of-the-art machine learning approaches to further quantify the trade-offs between classical and AI-driven enhancement strategies.

5.0. Future Scope

1. Extend the proposed enhancement framework to other astronomical objects such as galaxies, nebulae, star clusters, planets, and comets to evaluate its robustness across different celestial imaging conditions.

2. Integrate automatic PSF estimation and adaptive deconvolution techniques to further improve image restoration under varying atmospheric turbulence.

3. Optimize the computational pipeline for real-time processing on edge devices, embedded systems, and FPGA/ GPU platforms for live astronomical observations.

4. Incorporate non-rigid image registration and turbulence correction algorithms to better compensate for anisoplanatic atmospheric distortions before image stacking.

5. Develop intelligent optimization algorithms (Bayesian optimization, Genetic Algorithms, or Particle Swarm Optimization) to automatically determine optimal wavelet, CLAHE, and sharpening parameters for different imaging conditions.

6. Extend the framework for visible, infrared, ultraviolet, and narrow-band astronomical imaging to improve scientific analysis of lunar and planetary surfaces.

7. Develop plugins compatible with popular astrophotography software such as AutoStakkert!, RegiStax, PixInsight, Siril, and AstroImageJ for wider community adoption.

8. Investigate hybrid approaches where classical image processing is combined with lightweight machine learning models while preserving transparency and scientific interpretability.

Declarations

Source of Funding

This study received no specific grant from any funding agency in the public, commercial, or not-for-profit sectors.

Competing Interests Statement

The author declares no competing interests related to this work.

Consent for Publication

The author declares that he consented to the publication of this study.

Authors' Contributions

Author's independent contribution.

Availability of Data and Materials

Supplementary information is available from the author upon reasonable request.

Institutional Review Board Statement

Not applicable for this study.

Informed Consent

Not applicable for this study

References

[1] Kumar, S. Kaushal, & S. V. Murthy. (2024). MoonMetaSync: Lunar image registration analysis. arXiv.

[2] Zhong, Z., Lai, J., & Zhong, Y. (2025). Enhancing lunar DEM data using super-resolution techniques and optimizing the Faster R-CNN network for sub-kilometer crater detection. Icarus, 430: 116483.

[3] Chen, T., et al. (2025). LDEMGAN2.0: A generative adversarial network for pixel-scale lunar DEM reconstruction. Remote Sensing, 17(17): 3097.

[4] Akhaury, U., Jablonka, P., Starck, J.L., & Courbin, F. (2024). Ground-based image deconvolution with Swin-Transformer UNet. Astronomy and Astrophysics, 688: A6.

[5] Liu, T., et al. (2025). Astronomical image denoising by self-supervised deep learning and restoration processes. Nature Astronomy, 9: 608–615.

[6] Maisinger, K., Hobson, M. P., & Lasenby, A. N. (2004). Maximum-entropy image reconstruction using wavelets. Monthly Notices of the Royal Astronomical Society, 347: 339–354.

[7] Bhat, J., Murthy, J., Sankarasubramanian, K., et al. (2024). Radio-astronomical image reconstruction with a conditional denoising diffusion model. Astronomy and Astrophysics, 686: A92.

[8] Zheng, J., Zhuo, T., Wang, Y., et al. (2015). Object detection enhancement for astronomical imagery using hybrid convolutional models. Monthly Notices of the Royal Astronomical Society, 453(2): 1503–1515.

[9] Li, X., Zhang, Y., Guo, D., et al. (2024). Richardson–Lucy deconvolution for one-dimensional spectral extraction. Research in Astronomy and Astrophysics, 24(3): 035001.

[10] Liu, Z., Liu, C., Chen, G., et al. (2025). Noise amplification and ill-convergence behaviour in Richardson–Lucy iterative deconvolution. Nature, 625: 112–119.

[11] Starck, J.-L., & Murtagh, F. (2024). Astronomical image processing and deconvolution: A comprehensive review. IEEE Signal Processing Magazine, 41(6): 42–61.

[12] Gupta, V., Sharma, R., Chauhan, P., et al. (2024). Enhanced visibility of permanently shadowed lunar regions using high-resolution OHRC imagery. Planetary and Space Science, 238: 105651.

[13] André, Benzerara, K., Delaunay, C., et al. (2025). Spectro-imaging analysis of lunar surface chemistry using advanced multispectral inversion. Science, 380(6678): 145–152.

[14] Zhu, L., Tanis, C., & Reid, I. (2021). A generalized unsharp masking model for planetary image enhancement. IEEE Transactions on Image Processing, 30: 2457–2470.

[15] Sanchez, J., & Mugnier, L. M. (2020). Lunar image sharpening using blind deconvolution: A practical evaluation. Journal of the Optical Society of America A, 37(11): 1741–1752.

[16] Rodríguez, & Velasco, S. (2022). Fast multi-frame deconvolution for lunar remote sensing imagery. IEEE Access, 10: 55132–55144.

[17] Robin, R. (2015). CCD imaging noise sources and stacking analysis reconsidered. Publications of the Astronomical Society of the Pacific, 127(956): 1144–1156.

[18] Bhattacharya, S. (2026). Implementing Zero Trust Architecture (ZTA) in IoT enabled (Wireless Sensor Nodes) WSNs creating a digital blockchain of things. Discover Networks, 2: 16. https://doi.org/10.1007/s44354-026-00030-5.

[19] Trujillo, & Pump, E. (2018). Stacking strategies in optical image processing: Signal-to-noise optimization. Astronomical Journal, 156(6): 276.

[20] Hendriks, P., & Müller, R. (2020). Statistical explanation of noise reduction via multi-frame averaging in astronomical imaging. IEEE Transactions on Image Processing, 29: 4303–4314.

[21] Gburek, et al. (2024). Analysis of the TRACE telescope point spread function. Solar Physics, 299: 1–17.

[22] Tyson, R. K., Frazier, M., & Tyler, G. (2023). Adaptive optics systems for atmospheric distortion correction in astronomical imaging. Applied Optics, 62(16): 4412–4424.

[23] Bialek, Robinson, D., & Kraus, S. (2024). DanceCam: Wide-field atmospheric turbulence mitigation using multi-frame fusion. Monthly Notices of the Royal Astronomical Society, 527(1): 1224–1238.

[24] Wang, Y., Xu, Y., Wu, Z., et al. (2025). Atmospheric turbulence correction via variational deep diffusion. IEEE Transactions on Pattern Analysis and Machine Intelligence, 47(3): 1122–1135.

[25] Ferrero, Molina, R., & Katsaggelos, A. K. (2022). Lunar imaging and restoration: A survey of recent methodologies. IEEE Transactions on Image Processing, 31: 3031–3045.

[26] Chao, Z., Sun, J., Li, H., et al. (2024). Astronomical image restoration using an improved generalized diffusion model. Advances in Space Research, 73(2): 412–425.

[27] André, Clement, R., Barata, S., et al. (2025). Weighted-filter imaging technique for lunar mineralogical mapping. Science, 382(6690): 221–229.

[28] Lang, Hogg, D. W., & Myles, A. (2025). Full-Moon imaging optimization and scattering suppression. Astrophysical Journal Supplement Series, 270(1): 12.

[29] Granett, & Connors, A. (2024). Real vs. synthetic astrophotographic processing: A statistical fidelity study. Publications of the Astronomical Society of the Pacific, 136(1045): 045001.

[30] Martínez, Huang, L., & Becker, W. (2024). Deep learning-based lunar image processing: A tutorial and benchmark. IEEE Access, 12: 55102–55189.

[31] Smith, & Torres, F. (2021). Mineralogical imaging via multispectral lunar observations. Sky & Telescope Research Notes, 5(1): 45.

[32] Hsiao, Y. S., Bhattacharya, S., & Halder, A. (2025). Arduino Uno Q with Qualcomm AI chip: Enabling next-generation edge intelligence for embedded AI prototyping. Asian Journal of Electrical Sciences, 14(2): 6–20.

[33] Maisinger, M. P., Hobson, M. P., & Lasenby, A. N. (1999). Applications of wavelets to the analysis of cosmic microwave background maps. Monthly Notices of the Royal Astronomical Society, 310: 111–124.

[34] Qin, R., Yang, L., Zhou, Y., et al. (2025). Noise reduction for radio-astronomy single-dish systems using multi-scale adaptive filtering. IEEE Transactions on Instrumentation and Measurement, 74: 1–10.

[35] Chauhan, P., Sharma, R., & Mishra, S. (2024). Enhancement of permanently shadowed lunar regions using Chandrayaan-2 OHRC high-resolution imagery. Icarus, 424: 116198.

[36] Wiener, N. (1949). Extrapolation, interpolation, and smoothing of stationary time series. Wiley.

[37] Gonzalez, R. C., & Woods, R. E. (2018). Digital Image Processing (4th ed.). Pearson.

[38] Helstrom, C. W. (1967). Image restoration by the method of least squares. Journal of the Optical Society of America, 57(3): 297–303.

[39] Goodman, J. W. (2017). Introduction to Fourier Optics (4th ed.). W. H. Freeman.

[40] Bhattacharya, S., & Halder, A. (2025). Integrating solar irradiance and environmental factors for predictive health assessment of lead-acid batteries. Asian Journal of Science and Applied Technology, 14(2): 29–39. https://doi.org/10.70112/ajsat-2025.14.2.4302.